Liu et al. *Microsystems & Nanoengineering* (2025)11:192
https://doi.org/10.1038/s41378-025-01036-9

Microsystems & Nanoengineering
www.nature.com/micronano

ARTICLE Open Access

High-stability flexible thin-film temperature sensor using MWCNTs-toughened Peano structure

Zhaojun Liu[1,2,3,4]✉, Bian Tian[1,2]✉, Bogang Liu[1,2], Xiang Liu[1,2], Jiaming Lei[1,2], Jiangjiang Liu[1,2], Zhongkai Zhang[1,2], Chen Wu[1,2], Qijing Lin[1,5] and Zhuangde Jiang[1,2,5]

Abstract

Characterized by thinness, lightness and flexibility, flexible thin-film temperature sensors can be tightly fitted to different shapes of surfaces to measure their surface temperatures. However, the deformation in sensor installation and stress caused during temperature testing can lead to the deterioration in testing capability of the sensor. In this paper, the Peano structure is used to optimize the thin-film design for reducing the internal stress value. Additionally, multi-walled carbon nanotubes (MWCNTs) are doped into the thermoelectric material (Indium oxide, In_2O_3) to construct a powder-fiber staggered adhesive thin-film micro-structure, with the parameters involved in the co-conformal deposition of the thin-film optimized. Unaffected by force/deformation, a thermocouple-type flexible thin-film temperature sensor with high stability and reliability is developed. This sensor is considered promising for contact/non-contact (gas/liquid shock, etc.) measurement.

Introduction

As one of the important physical parameters widely used to characterize the state and properties of an object, temperature is indispensable in both production and life[1–5]. The constant advancement of micro-electro-mechanical system technology and flexible electronics is coupled with the evolution of temperature sensors from traditional thermocouples and thermal resistors to flexible thin-film thermocouples and thermal resistors. Flexible thin-film temperature sensors possess a series of significant advantages. Due to their excellent flexibility, the sensors can fit tightly onto the surface of objects with complex geometries, which not only significantly expands the scope of application for temperature monitoring but also improves the accuracy and adaptability of temperature measurement[6–9]. Secondly, the sensor design, which shows flexibility, can be customized according to the specific needs for temperature measurement, which allows a high degree of freedom in the measurement layout. It is an important measurement technology applied in biomedical, aerospace and other fields[10–15].

However, flexible thin-film temperature sensors are prone to deformation because of their high flexibility and adaptability, which is a key problem to consider for practical applications. Due to the inherent softness of the material, the sensors subjected to external forces or environmental changes are also prone to deformation, which compromises the accuracy of temperature measurement. Especially in complex or dynamic environments, there is a risk that the deformation of forces during installation and testing affects the physical properties of the electrodes, which results in significant temperature measurement errors[16–19]. For thermocouple-type flexible thin-film temperature sensor, common metallic materials (copper, silver, tungsten, rhenium alloys, etc.) are preferable for high ductility, but they perform poorly in test sensitivity (Seebeck coefficients) is low, making it difficult to detect slight temperature changes[10]. However, for the ceramic oxides with high Seebeck coefficients, such as In_2O_3, ITO, $La_{0.8}Sr_{0.2}CrO_3$, etc., it is difficult to achieve stable temperature measurement on flexible substrates due to brittleness and poor toughness[13,19–27].

Correspondence: Zhaojun Liu (lzj2024@xjtu.edu.cn) or
Bian Tian (t.b12@mail.xjtu.edu.cn)
[1]State Key Laboratory for Mechanical Manufacturing Systems Engineering, Xi'an Jiaotong University, Xi'An 710049, China
[2]School of Mechanical Engineering, Xi'an Jiaotong University, Xi'An 710049, China
Full list of author information is available at the end of the article

In order to solve the above-mentioned paradoxical problem arising from sensitivity and flexibility, it is proposed in this paper that the structural design, material combination and process can be optimized to obtain a thermoelectric flexible thin-film temperature sensor with high sensitivity and robustness to deformation/force. In structure, the thermo-electrode is designed with a Peano structure (arc angle of 270°), instead of the traditional linear structure. Regarding materials, the In_2O_3 powder particles with a high Seebeck coefficient are used as thermoelectric materials[13,20,26]. At a temperature below 400 °C, MWCNTs have excellent length-diameter aspect ratios (≈25 nm in diameter and ≈15 μm in length), high strength, high elasticity and stability[28–30]. A microstructure of powder-fiber staggered adhesion is formed by introducing MWCNTs as the connecting line between In2O3 powders. In terms of process, the content of MWCUTs is modulated while the process method is designed for the co-conformal preparation of thermoelectrode through the screen-printing process. The flexible thin-film temperature sensors with MWCNTs-toughened Peano structure are highly stable and reliable. Since it maintains a stable and continuous temperature measurement capability throughout the tensile and bend tests, the influence of the external environment can be ignored.

Simulation and fabrication

Before the preparation of flexible thin-film temperature sensor, thermoelectric and mechanical simulations are carried out for linear and Peano structures, respectively. AutoCAD is applied for two-dimensional model and Solidwork is adopted for three-dimensional model. Then, COMSOL is used for further analysis of properties.

During the thermoelectric simulation, the boundary conditions of the flexible sensors are set according to the actual test system and test conditions. As shown in Fig. S1a, there are four sensor structures established, including the linear structure and the Peano structure (with an arc angle of 90°/180°/270°)[31,32]. The terminal of the sensor (two cold pads) is set to 20 °C as the environmental temperature, and the temperature measuring end (overlap of two materials) is heated at different temperatures up to 360 °C. The left thermo-electrode is made of silver, and the right one is made of In_2O_3. Meanwhile, the terminal of the In_2O_3 thin film is grounded. As shown in Fig. S1a, b, there are no differences between all the structures in their static thermoelectric properties, including the temperature field and output thermal electromotive force. As shown in Fig. S1b, the maximal output thermal electromotive force is 51.2 mV, as measured by the probe in the terminal when the temperature difference reaches 340 °C between the temperature measuring end and the cold pads. According to the simulation results, the static thermoelectric characteristics of the flexible sensors are irrelevant to the structure of the thermo-electrodes[11].

When the flexible thin-film temperature sensor operates, it is inevitable that deformation occurs. In the process of mechanical simulation, the internal stress fields are simulated for the four structures of sensors under tensile deformation and compared according to the actual application state of the sensors. Given the superior ductility and toughness of the silver thermo-electrode to the In_2O_3 thermo-electrode, the cracks on the In_2O_3 thermo-electrode may lead to sensor failure in practice. Therefore, the sensitive layer material is set to In_2O_3 for comparing the mechanical properties of these four structures, as shown in Fig. S2a. During the course of simulated tensile deformation, a fixed constraint is applied to the upper surface of the substrate and a uniformly distributed load of 10–200 N downward/1–25% of the deformation is applied to the lower surface of the substrate. Figure S2b, c illustrates the distribution of internal stress. Obviously, the maximum internal stress of four structures is generated in the thermoelectric materials in close proximity to the terminal pads. Moreover, it is apparent that the Peano structure significantly reduces the internal stress generated in the structure under the same conditions. As the arc angle of the Peano structure increases, the internal stress declines continuously. Under the same conditions, the maximum internal stress of the Peano structure (with an arc angle of 270°) is reduced to 69.03% in comparison with the linear structure. By optimizing the structure of the thermo-electrode, the safety performance of the sensor in service has been improved to a significant extent.

Flexible polyimide thin film (75-μm thick) is taken as a flexible substrate for thin-film temperature sensors. However, it is difficult to achieve accurate pattern deposition due to its smooth surface and low roughness, which tends to cause the dispersion of paste in the screen-printing process. Thus, before the sensor is prepared, the inductively coupled plasma (ICP) technique is applied to bombard the surface of the flexible polyimide thin film. In the experiment, the radio-frequency power of 2200 W, the oxygen flow rate of 150Sccm and the working air pressure of 550μHg are applied to the surface of the polyimide. At the same time, argon is taken as a protective inert gas to physically clean the polyimide surface. An interval ventilation method is used, with 20 s of oxygen followed by 10 s of argon as a cycle. The ICP process is conducted on the flexible polyimide substrate for 300, 600, 900, and 1200 s, respectively. The polyimide surface is observed through confocal laser scanning microscopy and optical microscopy, as shown in Fig. 1a and Fig. S3, respectively. By analyzing the results of the confocal laser scanning microscopy test, as shown in Fig. S3a, the surface roughness-Ra of the original polyimide is 26 nm. After ICP etching treatment is carried out for different periods

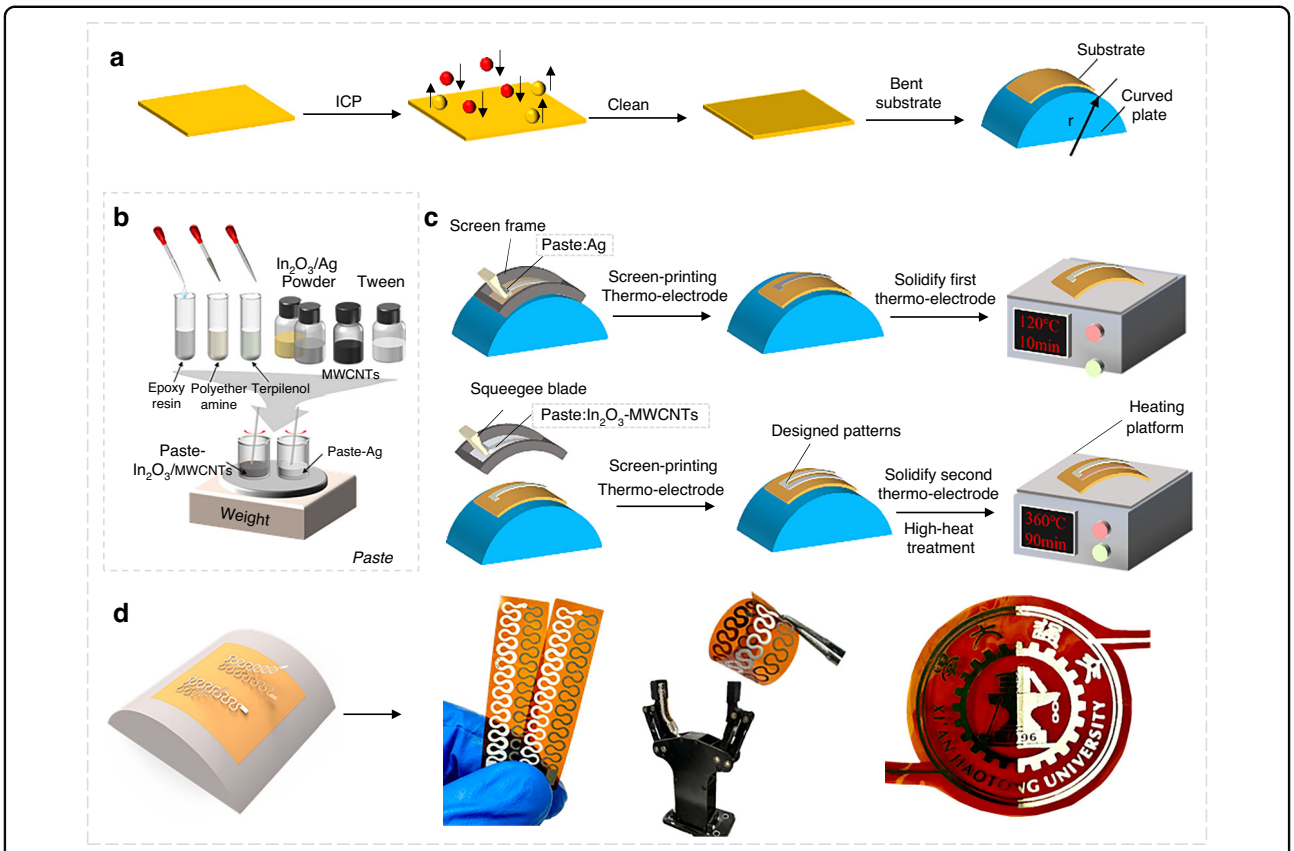

Fig. 1 The preparation process of the sensor and the diagram of the prepared sample. a Process of roughness improvement for flexible polyimide substrates. **b** Paste preparation in the screen-printing process. **c** The process of preparing the sensor by the screen-printing technology. **d** Flexible thin-film temperature sensor with Penao structure and customized university logo pattern

Table 1 The parameters of printing thermoelectric paste

Material	In_2O_3/Ag	MWCNTs	Tween	α-Terpineol	Epoxy resin	Polyether amine
Mass	1.50 g	0.00–0.10 g	0.00–0.10 g	0.30 g	0.60 g	0.32 g

of time, the roughness-Ra of polyimide thin film reaches 68 nm, 80 nm, 128 and 173 nm, respectively. Therefore, the surface roughness of the polyimide is substantially improved.

Moreover, the materials are proportioned according to the mass in Table 1 to obtain the slurries to be applied in the screen-printing process, as shown in Fig. 1b. The epoxy resin (E-51) and polyether amine (D-400) are respectively taken as the binder and curing agent to bond the thermo-electrode powder In_2O_3 and Ag, while α-Terpineol is treated as the thermal electrode powder solvent and curing catalyst[26,33]. Among them, six control experimental groups are set up by adding 0.00 to 0.10 g (0.02g-step) of MWCNT to In_2O_3 powder. The mass of Tween is maintained at the same level as the MWCNTs.

Figure 1c presents a schematic diagram of the screen-printing process. In the preparation process, the polyimide substrate is adhered to the curved surface. During operation, a printing side with a customized pattern is positioned on top of the polyimide substrate, with the patterned thermo-electrode deposition achieved by squeezing the configuration paste with a squeegee. To ensure the high quality and continuity of the thermo-electrodes, the electrodes are usually coated several times. After each printing, each thermo-electrode is heated at 120 °C for 10 min to ensure its complete curing on the heating platform. After the silver and In_2O_3 electrodes are sequentially prepared through the screen-printing process, the flexible thin-film temperature sensor is heat-treated at 360 °C for 90 min (and naturally cooled) to ensure thermal activation of the thermo-electrode

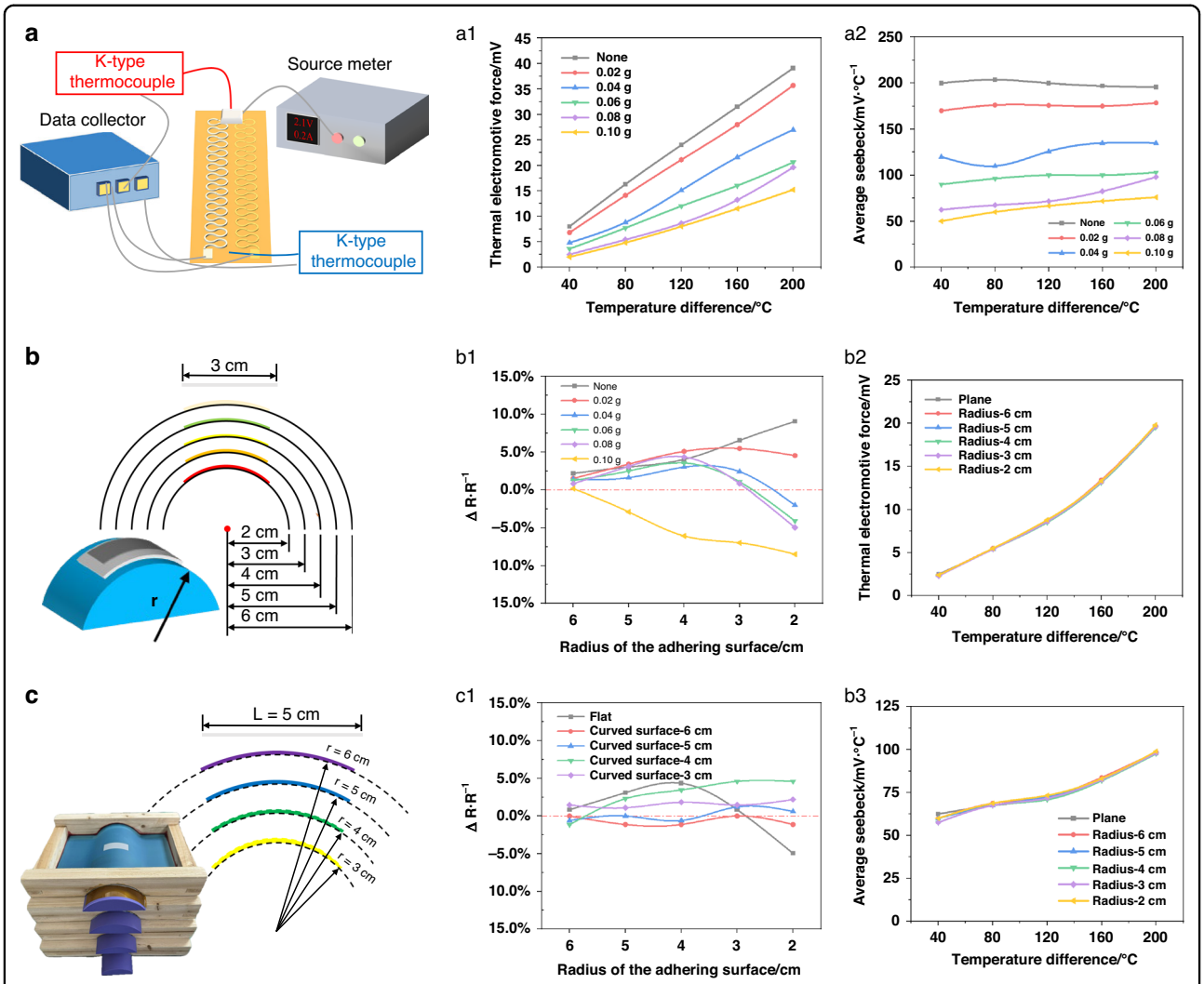

Fig. 2 Study on the co-conformal preparation process of In_2O_3-MWCNTs. a Thermoelectric and Seebeck coefficient test system for the flexible temperature sensor. **a**$_1$ Thermoelectric and **a**$_2$ Seebeck coefficient of In_2O_3-MWCNTs thermo-electrodes with different gradients. **b** Application of the thin films (In_2O_3 containing different mass fractions of MWCNTs) to a circular/flat surface with a radius of 2–6 cm. **b**$_1$ Resistance change rates of In_2O_3-MWCNTs thermo-electrodes under different curvature surfaces. **b**$_2$ Thermoelectric and **b**$_3$ Seebeck coefficient curves of In_2O_3-0.08gMWCNTs thermos-electrodes at different bending curvatures. **c** Co-conformal preparation process (flat surface, curved surfaces with a radius of 3–6 cm) based on screen-printing technology. **c**$_1$ Relative resistance change rates of In_2O_3-0.08 gMWCNTs thermo-electrodes prepared on the substrates with different bending curvatures

materials. Figure 1d displays the schematic and sample diagrams of the flexible temperature sensor with Peano structure as obtained by co-conformal preparation. Besides, the flexible temperature sensor with the customized university logo pattern (Xi'an Jiaotong University) is also illustrated. In the sample, the dark-colored electrode is In_2O_3 containing MWCNTs, and the light-colored one is a silver electrode.

In order to test and calibrate the In_2O_3-MWCNTs(0.00–0.10 g) thin film prepared for this study, a test system is developed, as shown in Fig. 2a. A K-type thermocouple is placed in the thermosensitive position to measure the temperature of the ceramic heater which is controlled and heated by changing the voltage and electricity of the source meter. The other K-type thermocouple is deployed to monitor the terminal side in real time. Besides, a data collector is used to record the temperature of the K-type thermocouples and the electromotive force of In_2O_3-MWCNTs(0.00–0.10 g) thin film. As shown in Fig. 2a$_1$, a$_2$ and Fig. S4a, the output thermal electromotive force of In_2O_3-MWCNTs thin film shows a decreasing trend with a rise in the content of MWCNTs in In_2O_3 powder (From In_2O_3: 39.1 mV@200 °C to In_2O_3-0.10gMWCNTs: 15.2 mV@200 °C). Also, there is a gradual decrease in the average Seebeck coefficient (From In_2O_3: 195.5 μV/°C@200 °C to In_2O_3-0.10gMWCNTs:

76.0 μV/°C@200 °C) and resistivity (From In_2O_3: 1.10 kΩ·cm to In_2O_3-0.10gMWCNTs: 0.48 kΩ·cm) of thin films. As the content of MWCNTs increases, the electrical conductivity of the In_2O_3 thin films is significantly enhanced. Meanwhile, the rise in the content of MWCNTs increases the number of microscopic interfaces. Similarly, the doping of MWCNTs increases carrier concentration, which reduces the Seebeck coefficient as a result[33–35].

The deformation resistance of the In_2O_3-MWCNTs thin films prepared under different process parameters is evaluated through a bending test. In general, the methods used to conduct bending test on the thin films deposited on the surface of flexible substrates are divided into three categories: Concentric axis experiment; Two-point bending experiment; The x-y-θ coordinate experiment[36–38]. Among them, the concentric axis experiment is the simplest one suitable to characterize the bending character of the samples based on the geometry of the cylinder. The process followed by this method is detailed as follows. A large number of identical specimens are attached to a series of cylindrical surfaces with different radii for concentric bending. Under similar operating conditions, the extent of influence from the deformation characteristics of the specimen is comparatively evaluated. The advantage of the concentric axis experiment lies in its simple operation. The bending curve of the samples is treated with a standard circle by attaching the samples to the outer surface of the cylinders, which allows the characteristics of the samples to be obtained quickly and conveniently. Apart from that, the calculation and processing of experimental data are simplified. As shown in Fig. 2b, the six sets of samples prepared in the experiment are cut into strips with a length of 3 cm and a width of 1 cm. Then, the samples are attached onto the flat and circular surfaces with a radius of 2–6 cm in turn, respectively. At this time, the multimeter is used to measure the resistance at both ends along the length of the samples. Afterwards, the resistance of the unbent In_2O_3-MWCNTs thin film on the flat is taken as the reference resistance. The relative change in the resistance of the In_2O_3-MWCNTs thin films on different circular surfaces is taken as the factor to be used for evaluating the resistance of the film to deformation[39].

As revealed by comparing the test results shown in Fig. 2b_1, b_3 and Fig. S5, increasing the content of MWCNTs is an effective solution to the problem that the internal destruction of In_2O_3 thermo-electrode increases resistance and significantly reduces the thermoelectric output when the thermo-electrode is attached to a large curvature surface. Sharp curvature induces localized strain fields and atomic disorder at interfaces, creating additional scattering centers for charge carriers. Meanwhile, as shown in Fig. S5, the thermal electromotive force and Seebeck coefficient of the In_2O_3-MWCNTs thermo-electrodes are unaffected by bending deformation when the content of MWCNTs exceeds 0.08 g. Taking into account both the sensitivity of the thermo-electrode and the resistance to deformation, the In_2O_3 containing 0.08g of MWCNTs is selected for the subsequent test. For the In_2O_3-0.08gMWCNTs material, the maximum voltage variation and the Seebeck coefficient variation is only 6.5% during the test. The thermoelectric properties of In_2O_3-0.08gMWCNTs thin films are almost no longer affected by the shape of the attached surface. Fig. S6 also shows the output comparison of two batches of In_2O_3-0.08gMWCNTs sensors. The maximum precision error between the two batches is 2.32%, demonstrating great consistency.

In order to further improve the performance of the In_2O_3-0.08gMWCNTs thin film in resisting deformation under the optimal process preparation parameters, a co-conformal preparation method is proposed, in which the substrate is bent through the screen-printing technology to different degrees before preparation. When the In_2O_3-0.08gMWCNTs thermo-electrode is prepared on the surface of a circle with a diameter of 12 cm and placed on the surface of a circle with a diameter of more than 12 cm for measurement and use, the thermo-electrode is equivalent to the state under pressure, for which the occurrence of deformation has little effect on its characteristics. Therefore, before the substrate is placed under the screen-printing frame, the flexible substrate is adhered to a curved surface (radius of 3–6 cm) with the same curvature as the frame, which facilitates co-conformal preparation. As shown in Fig. 2c–c_1, a co-conformal surface with a radius of 6 cm is selected for the deposition of the In_2O_3-0.08gMWCNTs thin film, considering the results of the resistivity change test and the feasibility of the actual preparation process.

Characterization

Given the optimization results of the material ratios and the co-conformal preparation process, a scanning electron microscope (SEM) with the in situ stretching function is employed to observe the changes in the microscopic properties of the thin films (between In_2O_3 and In_2O_3-0.08gMWCNTs).

As shown in Fig. 3 and Figs. S7, S8, the cured In_2O_3 thin films containing different MWCNTs is consistent in microscopic morphology, with all of the powder-fibers completely encapsulated by the cured epoxy resin. However, compared to the In_2O_3 microscopic morphology shown in Fig. 3a_2, a_3, the MWCNTs in Fig. 3b_2, b_3 and Fig. S7b–f are uniformly entangled around the In_2O_3 powder following the heat treatment performed at 360 °C, which leads to a powder-fiber staggered adhesive microstructure. As can be observed from Fig. 3a_4, a_5, b_4, b_5

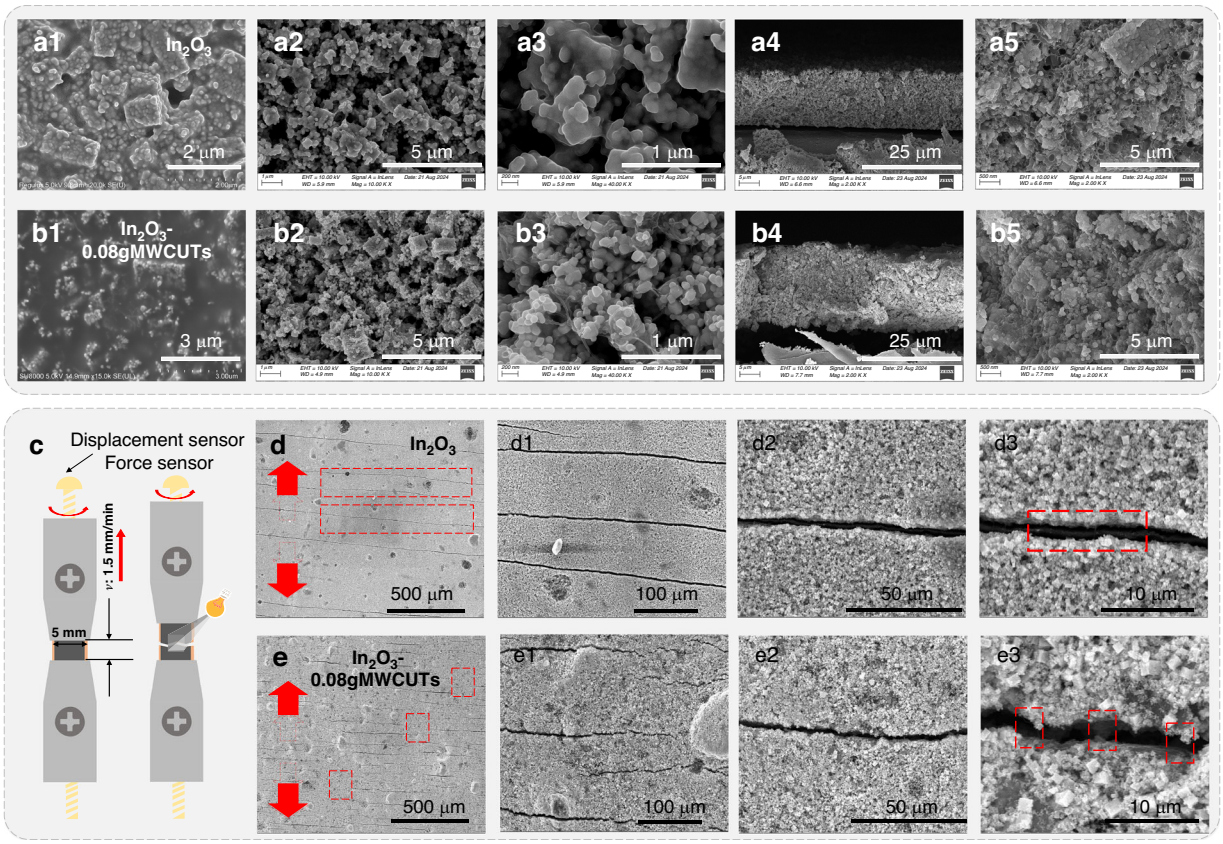

Fig. 3 The SEM images of the surface of In_2O_3 and In_2O_3-0.08gMWCNTs thin films. $\mathbf{a}_1$–$\mathbf{b}_1$ The surface of the thin films obtained after curing at 120 °C. $\mathbf{a}_2$–$\mathbf{a}_3$, $\mathbf{b}_2$–$\mathbf{b}_3$ The surface of the thin films obtained after heat treatment at 360 °C. $\mathbf{a}_4$–$\mathbf{a}_5$, $\mathbf{b}_4$–$\mathbf{b}_5$ The cross sections of thin films obtained after heat treatment at 360 °C. **c** Schematic diagram of the stretching process of the micro-tensile machine observed by SEM. **d**–$\mathbf{d}_3$ Detailed view of the stretching process of In_2O_3 thin film. **e**–$\mathbf{e}_3$ Detailed view of the stretching process of In_2O_3-0.08gMWCNTs thin film

and Fig. S8, the thin films deposited by the screen-printing technique have favorable densification without large internal voids and defects. Also, according to the Energy dispersive spectrometer (EDS) elemental distribution illustrated in Fig. S9, the elements are uniformly distributed. After heat treatment at 360 °C, the solidified mixture pyrolyzes to form carbon and carbon oxides. Specifically, the solid product of pyrolysis acts as a binder for the thermal electrode powders, maintaining the integrity and connectivity of the thin film. In the meantime, the MWCNTs in the In_2O_3-0.08gMWCNTs thin film is volatilized by heat and disappear after the heat treatment carried out at 700 °C, as shown in Fig. S10. Therefore, the upper limit does not exceed 700 °C for the service temperature of the In_2O_3-0.08gMWCNTs thin film.

In fact, the form of the cracks can directly indicate qualitatively the fracture toughness of the thin films. The formation of small cracks is usually indicative of localized yielding or microdamage of the material under stress, but the cracks are effectively suppressed, deflected, or bridged, and fail to penetrate the entire cross-section. On the contrary, the appearance of large penetrating cracks is a typical characteristic of brittle fracture, indicating that the material is weak in its ability to resist crack initiation and propagation, and that once cracked, it is rapidly destabilized and expanded. Overall, the addition of MWCNTs significantly improved the toughness and fracture resistance of the In_2O_3 material thin films. The fine crack network exhibited during the stretching process of the MWCNTs-containing thin films is direct evidence of their higher fracture toughness and damage tolerance. Therefore, the mechanical properties of In_2O_3-MWCNTs are superior to those of the original In_2O_3 material films.

To further observe the fracture behavior of the In_2O_3 and In_2O_3-0.08gMWCNTs thin films, an in-situ SEM tensile system is adopted to test the mechanical properties of the thin films for comparative experiments. As shown in Fig. 3c and Fig. S11a, b, a systematically set external force is applied to the two thin films, while the force and displacement sensors inside the device are used to provide real-time feedback.

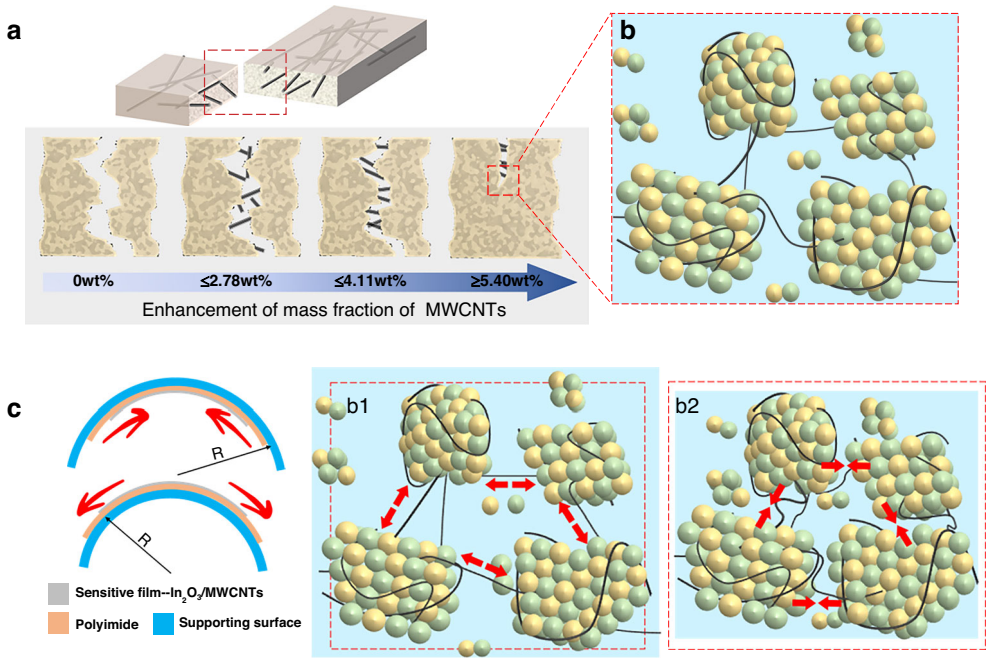

Fig. 4 Schematic diagram of thin film crack extension. a Changes in the form of thin film cracks with an increase in the content of MWCNTs. **b** Schematic diagram of powder-fiber staggered adhesive micro-structure. **b**$_1$ Thin-film micro-structure under tensile stress. **b**$_2$ Thin-film micro-structure under compressive stress. **c** Schematic diagrams of the two cases of structural forces in practical applications

The maximum deformation of the sensor fatigue test is shown in Fig. S12. According to the comparison shown in Fig. 3d, e and Fig. S11c, there are different forms taken by the cracking that occurs in the thin films. For the In_2O_3 thin film under 400 N stress, the film shows a large number of penetrating cracks in the direction perpendicular to the stretching direction, exposing the polyimide substrate in Fig. 3d$_3$ directly. On the contrary, the In_2O_3-0.08gMWCNTs thin film shows fine cracks at higher stresses and the cracks are found to be twisted. As shown in Fig. 3e$_3$, there remain multiple powder-fiber connections inside the cracks, which prevent the complete fracture of the In_2O_3-0.08gMWCNTs thin film[40,41].

From Figs. 2b$_1$, b$_2$, 3, it can be seen clearly that the incorporation of MWCNTs effectively improves the poor toughness, easy fracture, and instability of In_2O_3 thin film. Additionally, the In_2O_3-MWCNTs thin films exhibit high mechanical stability with the continuous increase of MWCNTs content. As shown in Fig. 4a, b, the incorporation of MWCNTs enhances the physical connection between In_2O_3 powders. The MWCNTs with a large length-diameter ratio act as “steel bars” and the In_2O_3 powder acts as “concrete”, which leads to an effective micro-structural combination. Due to the pulling of MWCNTs fibers with excellent mechanical properties, the extension of cracks is effectively inhibited. Therefore, the thin film is subjected to tensile force and pressure in use, as shown in Fig. 4c. According to Fig. 4b$_1$, the MWCNTs entangled in the In_2O_3 powder exhibit a traction function when tensile force acts on the In_2O_3-MWCNTs thin films. This not only maintains a reliable connection between the powders but also prevents the thin film from penetrating the fracture and functional failure. Ultimately, the extension of cracks is effectively inhibited. When the In_2O_3-MWCNTs thin films are subjected to pressure, the MWCNTs show relaxation, and the film properties are unaffected.

Experiment and test

Through the system illustrated in Fig. 2a, the fatigue resistance of In_2O_3-0.08gMWCNTs thermo-electrode is investigated by reciprocating the screw. As shown in Fig. 5a, b, systematic fatigue tests are performed on the In_2O_3-0.08gMWCNTs thermo-electrode. According to Fig. 5a–a$_2$, the resistivity change rate of the In_2O_3-0.08gMWCNTs thermo-electrode changes periodically with the reciprocating motion of the screw, but the maximum value of the resistance change rate is merely 5.0%. The thin film remains intact throughout the fatigue test, showing no sharp increase in resistance. The characteristics of the prepared thermo-electrode are further explored by continuously collecting the thermal electromotive force of the In_2O_3-0.08gMWCNTs thin film on the reciprocating screw. As indicated by the results presented in Fig. 5b, the In_2O_3-0.08gMWCNTs thermo-electrode performs well in working reliability and

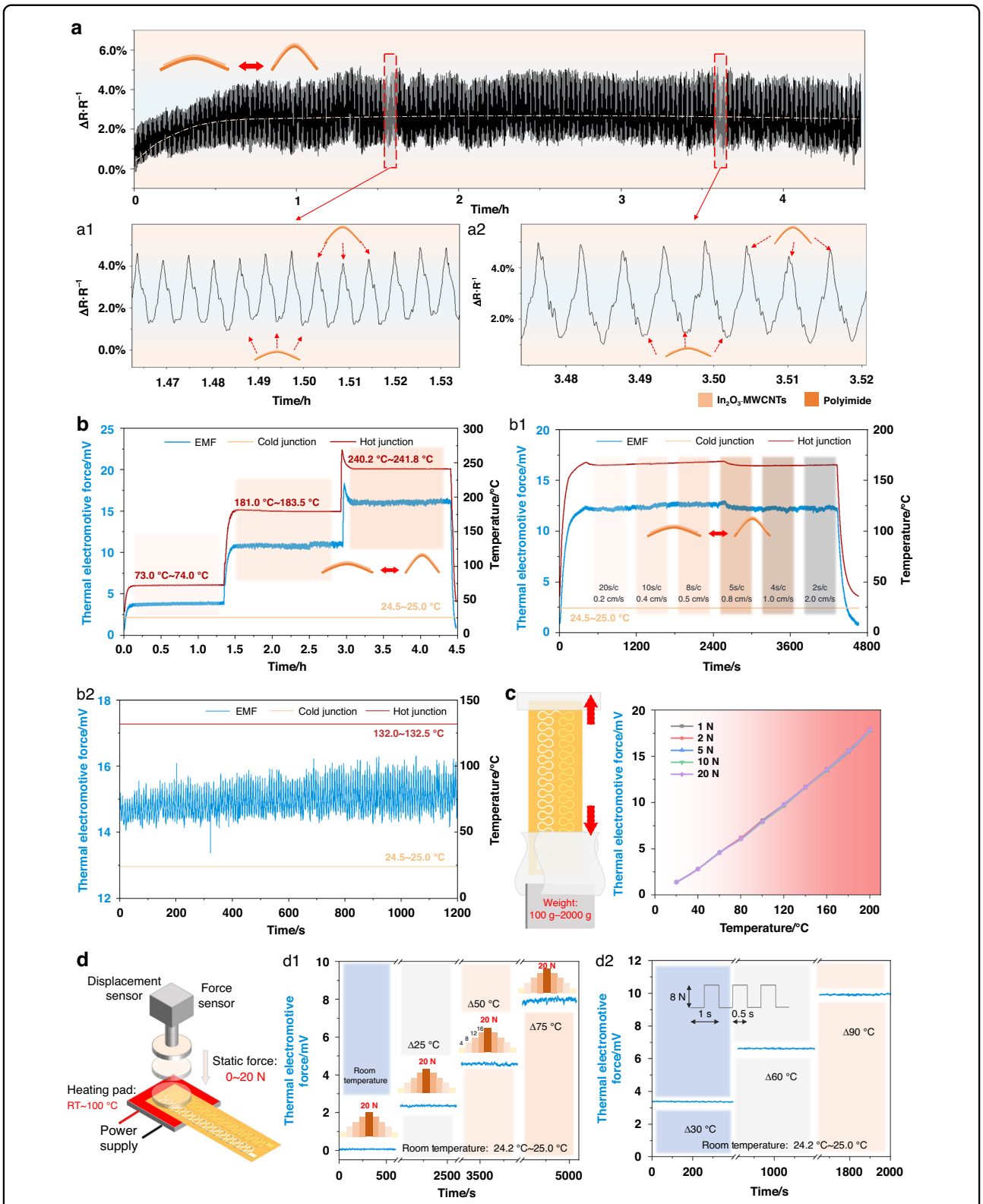

Fig. 5 (See legend on next page.)

(see figure on previous page)
Fig. 5 Practical test on the force/deformation resistance of flexible temperature sensors. a–**a**$_2$ Durability test of In_2O_3-0.08gMWCNTs thermo-electrode by multiple strain cycles. **b** The thermoelectric output curve of the In_2O_3-0.08gMWCNTs thermo-electrode under the reciprocating motion of the lead screw. **b**$_1$ Thermoelectric output curve of the In_2O_3-0.08gMWCNTs thermo-electrode at different reciprocating speeds of the lead screw. **b**$_2$ Thermoelectric output curve of the In_2O_3 thermo-electrode under the reciprocating motion of the lead screw. **c** The service characteristics of the In_2O_3-0.08gMWCNTs thermo-electrode under different tension conditions. The force of gravity exerted by the standard weight is taken as a pull on the sensor. **d** Application of static/cyclic pressure to the temperature sensor during the temperature test. Test on the stability of the sensor in contact temperature measurement. The thermoelectric output curve of the In_2O_3-0.08gMWCNTs thermo-electrode under **d**$_1$ different static force and **d**$_2$ cyclic force tests

temperature retention, and it can work continuously for hours. When the test temperature reaches 73–74 °C, 181–183.5 °C, and 240.2–241.8 °C, the temperature drift rate of the flexible temperature sensor is 11.6, 10.6, and 10.1 °C/h, respectively. Because of the insignificant temperature drift rate, the measurement accuracy and stability of the sensor are ensured in the presence of deformation. During the test, the reciprocating speed of the screw (From 0.2 to 2.0 cm/s) changes and the temperature measurement end is maintained at ≈170 °C, as shown in Fig. 5b$_1$. From these results, the thermoelectric properties of the flexible temperature sensor are unaffected by the degree and rate of deformation. Similarly, fatigue tests are performed on the unoptimized In_2O_3 thermo-electrode, as shown in Fig. 5b$_2$. The unoptimized In_2O_3 thermo-electrode shows large jumps in the voltage signal with a temperature drift of 20.0 °C/h.

On the other hand, an investigation is conducted into the thermoelectric characteristics of the sensor under different tensile forces. In order to quantify the applied force, an experiment is conducted with a series of standard weights as the force source, as shown in Fig. 5c. After the sensor is placed vertically on the ground for the experiment, its upper end is fixed, and the weight is fixed on the lower end surface of the sensor with adhesive tape. Then, the sensor is tested by the system shown in Fig. 2a again. The experimental results presented in Fig. 5c show the excellent tensile properties exhibited by its overall structure. According to the simulation results in Fig. S2c, the maximum internal stress in the sensitive thermo-electrodes of the sensor shows a positively correlated increase under the tension of 0–20 N as the tensile force increases, but the high stability and reliability of the sensor are maintained.

Meanwhile, the size of the heated ceramic plate in Fig. 2a increases according to the static test system. As shown in Fig. 5d, the temperature measuring end of the In_2O_3-0.08gMWCNTs thermo-electrode is attached to the heated ceramic plate, with static/cyclic force applied to it. As can be seen from Fig. 5d$_1$, the temperature of the ceramic plate varies when the current and voltage of the power supply output change, with different static forces (0–20 N) applied during the temperature holding phase. Although the thermal electromotive force of the temperature sensor fluctuates to a lesser extent in the low temperature range, there is a slight increase in the magnitude of fluctuation as the temperature gradient rises. This is attributed to the effect of heat transfer from the load module, which adversely affects the temperature retention of the test system. The maximum temperature fluctuation at each stage is: 0.1 °C(Room temperature), 0.6 °C(Δ25 °C), 0.9 °C(Δ50 °C) and 1.6 °C(Δ75 °C). Meanwhile, cyclic forces are applied to the sensor at different temperature gradients. With a rectangular signal as the input mode for the cyclic force, a period of 1 s is set, a duty cycle of 50% is set, and the force is set to 8 N. The maximum temperature fluctuation at each stage is as follows: 0.5 °C(Δ30 °C), 0.5 °C(Δ60 °C), and 0.6 °C(Δ90 °C). After multiple rounds of deformation/force fatigue test, the flexible thin-film temperature sensor consisting of In_2O_3-0.08gMWCNTs and silver electrodes is found to remain structurally intact and be capable of achieving stable temperature detection under various complex conditions, which is unaffected by force/deformation. Thus, the sensor ensures high test sensitivity (average Seebeck coefficient: 99 μV/°C) while showing robustness to external forces/deformations during testing. Fig. S14 shows the rate of change of sensor resistance as obtained at different temperatures and under different static forces. The overall resistance change rate of the sensors is less than 2.0%, which is insignificant.

Static tests are carried out on the prepared flexible In_2O_3-0.08gMWCNTs/Ag thin-film temperature sensor, as shown in Fig. 6a$_1$–a$_3$. The temperature measurement end is heated and cooled in multiple cycles to calculate the repeatability error and the relationship between temperature difference and thermal electromotive force. According to the calculation results, the maximum standard deviation of five cycles is 1.06 mV, and the repeatability error is ±5.04%. Equation 1 describes the relationship between temperature difference and thermal electromotive force (TEMF)[11,21].

$$TEMF = 0.000226 \times (\Delta T)^2 + 0.0570 \times (\Delta T) + 0.609 \quad (1)$$

The maximum TEMF can even increase to 21.09 mV when the temperature measurement end is 224.5 °C and

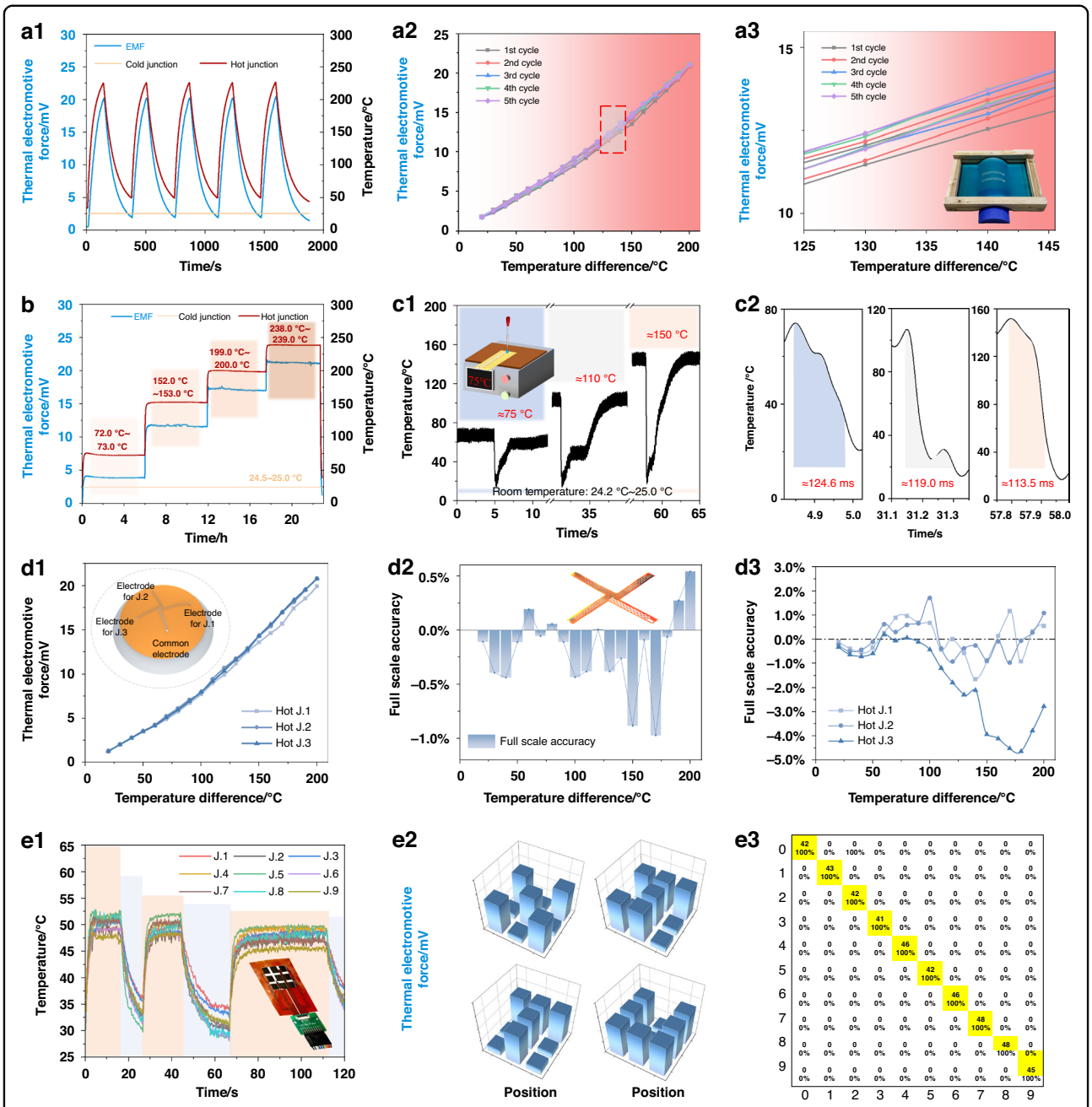

Fig. 6 Basic characterization tests of the flexible temperature sensor. $\mathbf{a}_1$–$\mathbf{a}_3$ Evaluation of test repeatability for flexible thin-film temperature sensors (In_2O_3-0.08gMWCNTs/Ag). **b** The temperature retention performance of the sensor at different temperatures. $\mathbf{c}_1$, $\mathbf{c}_2$ Test on the speed of sensor response by using anhydrous ethanol volatilization. $\mathbf{d}_1$–$\mathbf{d}_3$ Precision calibration method by multi-junction. $\mathbf{e}_1$–$\mathbf{e}_3$ Performance test on 3 × 3 arrays of flexible thin-film temperature sensors

the cold junction is room temperature (24.5 °C). The average Seebeck coefficient of the flexible In_2O_3-0.08gMWCNTs/Ag thin-film temperature sensor reaches 105.05 μV/°C, which enables the detection of slight temperature changes. The maximum hysteresis error is 3.01% (at 120 °C) of the full range. Similarly, the temperature retention of the sensor is tested and calculated using Equation S2. When the test temperature is 72–73°C, 152–153.0 °C, 199.0–200.0 °C and 238–239.0 °C, the temperature drift rate of the flexible temperature sensor is 1.86, 2.33, 3.41, and 3.32 °C/h, respectively. In contrast to Fig. 5b, the temperature retention performance of the sensor is unaffected by the state of cyclic deformation.

With the static characteristics of the sensor determined, the drop method is used to shock the temperature measurement end of the sensor to test the dynamic response time through the drop-volatilization of the liquid (Anhydrous ethanol). To conduct three tests, the temperature of the heating table is set to ≈75, ≈110, and ≈150 °C, while the state of the system is kept stable. When anhydrous ethanol drops to the temperature measurement site, it undergoes rapid heat absorption and volatilization, which causes a significant and rapid decline in TEMF of the sensor, as shown in Fig. 5c_1, c_2. In the three measurements, the time for the TEMF to reach 63.2% of the decrease in amplitude is 124.6, 119.0, and 113.5 ms, respectively, which is considerably faster than the response time of a conventional thermocouple(≈0.5 s)[42].

Defined as the measurement accuracy of a flexible thin-film thermocouple at the maximum range of its measurement range, full-scale accuracy represents one of the critical parameters required to evaluate the accuracy of a sensor in temperature measurement. Full-scale accuracy is usually expressed as a percentage or as a specific numerical value used to indicate the maximum error between the output value of a flexible thin-film thermocouple and its actual value. As shown in Fig. 6d and Fig. S13, a signal segmentation fitting method based on an arrayed temperature measurement structure is proposed to improve the sensor testing accuracy for the calculation of the full-scale accuracy achieved by a flexible thin-film temperature sensor. For flexible thin-film temperature sensors, the temperature range of the sensor is divided into multiple temperature segments under the method, with each segment fitted separately to obtain a more accurate temperature output value. Figure. 6d_1 shows the temperature-TEMF relationship curves obtained separately for each temperature measurement end of the array sensor. Figure. 6d_2 shows the full range error curve of the flexible thin-film temperature sensor after accuracy calibration. When the divided temperature interval length is 10 °C, the maximum full range error of the sensor is close to ±5.0%FS in the range of 20–200 °C. However, when optimized using a three-junction accuracy calibration method, the maximum full-scale error of the array sensor is only ±0.97%FS, as shown in Fig. 6d_3[43]. For the thermal noise (Johnson-Nyquist noise), the resistance of the sensor is 816.6 Ω. The thermal noise is calculated as 4.618 nV when the frequency bandwidth is 1 kHz and the temperature is 200.1 °C, equal to 473.25 K. For SNR (signal-to-noise ratio, dB), which is the ratio of signal power to noise power, it's 93.01 dB, which is large enough to have a clear signal. The minimum detectable temperature is 0.00014 °C in theory. The resistance of the sensor is measured by a multimeter (2000, Keysight, USA).

Furthermore, the flexible temperature sensor of an array type is designed and prepared for temperature detection over a certain area. This sensor adopts the common-ground principle, with only N + 1 wires required for N temperature measurement points. Figure S15 displays the screen-printed stencil of the designed arrayed flexible temperature sensor. Figure. 6e_1 illustrates the temperature detection of a beaker containing hot water, reflecting the imperceptible change in the temperature of the hot water in the beaker decreasing over time. A temperature stimulation test is performed at some temperature points of the array temperature sensor to capture the pixel images of the maximum TEMF at nine temperature measurement ends. As shown in Fig. 6e_2, the array sensor has high temperature resolution, which enables the regional temperature detection of non-uniform-temperature fields. At the same time, the use of array sensors makes it possible to collect data from multiple temperature measurement channels simultaneously. The multi-channel data is efficiently processed by a convolutional neural network algorithm, with features automatically extracted from the data to recognize the shape of the structure. As shown in Fig. 6e_3, the array sensor structure is adopted to accurately recognize the stimulus with the temperature of the digits "0-9"[44–46].

Practical temperature measurement tests are conducted on the prepared flexible In_2O_3-0.08gMWCNTs/Ag thin-film temperature sensors. As shown in Fig. 7a, systematic tests are carried out for different heat transfer media and heat transfer methods. Firstly, the temperature detection performance of the sensor for gas is tested. A hot blower is adopted as the load to apply temperature, and the air outlet of the blower is made to point to the temperature measurement end of the sensor for the collection of the temperature data. According to the results shown in Fig. 7b, the temperature signal of the sensor increases slowly and remains stable with the temperature under the continuous action of the hot air blower. Additionally, the corresponding temperature test results are obtained with the change of the hot air blower in different power modes, which suggests that the flexible sensor ensures reliable operating characteristics consistently during the thermal convection test of gases. Next, the flexible sensor is subjected to multiple temperature increasing and decreasing tests conducted with a radiant electric heater, as shown in Fig. 7c. According to Fig. 7c, the temperature intensity detected by the sensor changes constantly with the continuous variation of thermal radiation intensity, which demonstrates the excellent performance of the sensor in thermal radiation temperature measurement.

Moreover, flexible sensors are used to test heat conduction in liquids, as shown in Fig. 7d_1–d_3. Firstly, the sensor is attached to the inner wall of the self-heating lunchbox in Fig. 7d_1. After the addition of water to the self-heating pack, the sensor is used to detect the temperature change of the lunchbox. There is a large amount

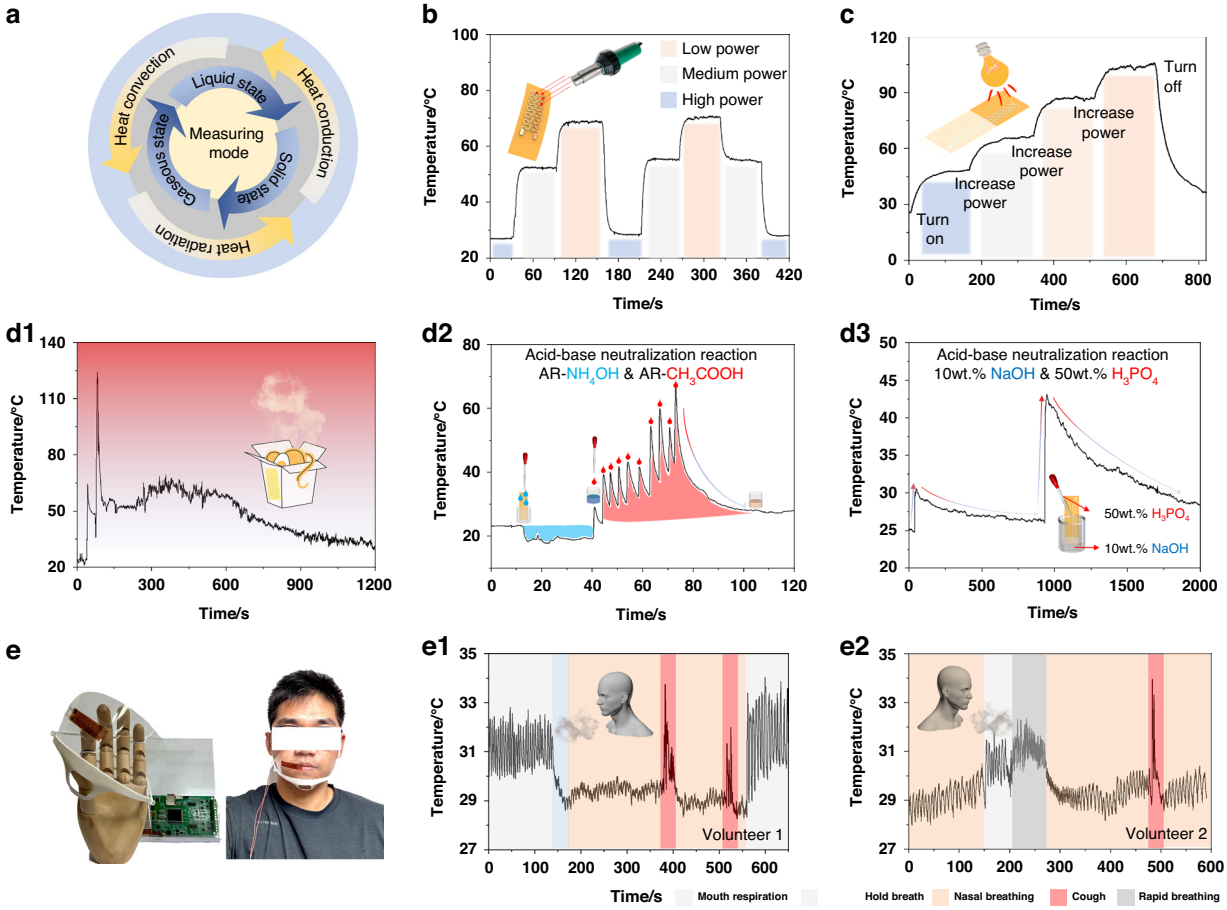

Fig. 7 Comprehensive evaluation of the flexible temperature sensor. a Different measurement modes: solid state, gaseous state, liquid state; heat conduction, heat convection, and heat radiation. **b** Gaseous state-heat convection: airflow temperature detection of hot air welding machine. **c** Heat radiation: temperature detection of electric heaters based on heat radiation. **d** Liquid state-heat conduction: $\mathbf{d}_1$ heating pack temperature detection for self-heating lunch boxes. $\mathbf{d}_2$, $\mathbf{d}_3$ Monitoring of the real-time changes in the temperature of the acid-base neutralization reaction. **e** Smart mask, a wearable device for human respiratory status monitoring. $\mathbf{e}_1$, $\mathbf{e}_2$ Gaseous state-heat convection: multi-mode breathing state detection and differentiation for different wearers

of heat released immediately when various materials, such as calcium oxide and aluminum powder in the heating package, come into contact with water. The sensor detects a maximum temperature of up to 125 °C. Given the ultra-high sensitivity of the sensor and its applicability to measure the temperature of liquids, the sensor is used in this study to detect the process of chemical reactions. The degree of chemical reaction is evaluated in real time by detecting the change in the temperature of the solution due to the endothermic heat during the reaction. In line with the aforementioned principle, reactions (e.g., neutralization reactions and most chemical reactions) can be monitored in real time, and the degree of chemical reactions can be reflected by the level of physical information. Figure. 7d_2, d_3 presents the data obtained by dropping CH_3COOH(AR) into the NH_4OH(AR) solution via a plastic dropper. In this study, the heat release data of the acid-base neutralization reaction are collected using the flexible temperature sensor attached to the inner wall of the beaker. When there is only NH_4OH solution in the beaker, its volatility at room temperature causes a decline in the temperature of the beaker. After the CH_3COOH solution is dropped into the NH_4OH solution, a rapid reaction occurs and a large amount of heat is released, which causes a sharp rise in the temperature. The sensor is applicable to record both rapid response processes quickly and consistently. Likewise, the sensor can also be used to record the acid-base neutralization reaction of a 10 wt% NaOH drop into 50 wt% H_3PO_4. When the alkaline solution is added dropwise into the acidic solution, a large-scale release of heat also occurs for a short period of time. The acidic solution surrounding the drop of alkaline solution is diluted, which slows down the reaction process. However, the chemical reaction continues with the

constant diffusion of molecules, and the solution continues to be diluted. The cycle of this process leads to the constant fluctuation in temperature of the solution in the overall downward trend. During chemical reactions, the combination reaction and acid-base neutralization reaction are mostly accompanied by the absorption and release of heat. Through this sensor, the real-time monitoring of chemical reactions can be achieved, which makes a non-visualized process a visible physical parameter.

The sensor can also be applied in smart wearable devices to acquire more biological information more effectively. As shown in Fig. 7e$_1$, the sensor is combined with an environmental-friendly transparent mask to monitor the breathing state of the human body in real time, which is based on convective heat exchange and temperature measurement. Figure. 7e$_2$, e$_3$ presents the monitoring results of the different human body in different breathing states. The different responses of the sensors can be intuitively compared under different respiratory states, e.g., nose breathing, mouth respiration, breath-holding, coughing, etc. Through the collection and processing of data, the mask is expected to be useful to monitor sleep apnea syndrome (SAS) via sleep snorers, with timely warnings and reminders issued for long-term apneas. With the timely feedback of sensors, early detection, early intervention and early treatment can be achieved for the health of the human body[12–15,47,48].

Conclusion

In this study, a flexible temperature sensor which can ignore the effects of external deformations/forces is designed and fabricated, with its performance evaluated comprehensively. Also, experimental tests are carried out in a variety of different force/deformation environments. The optimized In_2O_3-MWCNTs thin film is used to construct a powder-fiber staggered adhesive thin-film micro-structure, with a balance achieved between mechanical properties and thermoelectric properties. Moreover, the fabricated flexible temperature sensor is found capable of monitoring the temperature of different heat transfer methods and different heat transfer media.

Acknowledgements
This work is supported by Yangtze River Delta (Bengbu) Industry-Education Integration and Collaboration Center of State Key Laboratory for Manufacturing Systems Engineering, National Natural Science Foundation of China (52293405, 52505633), AVIC Industry Academia-Research Cooperation Project(HFZL2023CXY011), Postdoctora Innovative Talent Program of China (BX20240278), China Postdoctoral Science Foundation (2025M773615), Key Laboratory for Precision/Non-traditional Machining and Micromanufacturing Technology of Ministry of Education Open Project Fund, Dalian University of Technology (B202503). The authors would like to thank Dan He at the Instrument Analysis Center, Xi'an Jiaotong University, for her assistance with Fourier infrared spectrometer analysis.

Author details
[1]State Key Laboratory for Mechanical Manufacturing Systems Engineering, Xi'an Jiaotong University, Xi'An 710049, China. [2]School of Mechanical Engineering, Xi'an Jiaotong University, Xi'An 710049, China. [3]State Key Laboratory of High-performance Precision Manufacturing, Dalian University of Technology, Dalian 116024, China. [4]Key Laboratory for Micro/Nano Technology and System of Liaoning Province, Dalian University of Technology, Dalian 116024, China. [5]School of Instrument Science and Technology, Xi'an Jiaotong University, Xi'An 710049, China

Author contributions
Zhaojun Liu proposed the sensor design and wrote the manuscript. Bogang Liu and Xiang Liu assisted in the experiment setup design and sensor design. Jiaming Lei and Jiangjiang Liu assisted in writing and correction of the manuscript. Chen Wu, Qijing Lin, and Zhuangde Jiang gave technical support in the device design and fabrication.

Conflict of interest
Zhuangde Jiang is an Editor for the journal; no other author has reported any competing interest.

Supplementary information The online version contains supplementary material available at https://doi.org/10.1038/s41378-025-01036-9.

Received: 30 March 2025 Revised: 29 July 2025 Accepted: 10 August 2025
Published online: 23 October 2025

References

1. Huang, S. et al. Flexible electronics: stretchable electrodes and their future. *Adv. Funct. Mater.* **29**, 1805924 (2019).
2. Yokota, T. et al. Ultraflexible, large-area, physiological temperature sensors for multipoint measurements. *Proc. Natl Acad. Sci. USA* **112**, 14533–14538 (2015).
3. Salvatore, G. A. et al. Biodegradable and highly deformable temperature sensors for the internet of things. *Adv. Funct. Mater.* **27**, 1702390 (2017).
4. Shin, J. et al. Sensitive wearable temperature sensor with seamless monolithic integration. *Adv. Mater.* **32**, 1905527 (2019).
5. Nag, A. et al. Graphene-based wearable temperature sensors: a review. *Mater. Des.* **221**, 110971 (2022).
6. Zhang, F. et al. Flexible and self-powered temperature–pressure dual-parameter sensors using microstructure-frame-supported organic thermoelectric materials. *Nat. Commun.* **6**, 8356 (2015).
7. Zardetto, V. et al. Substrates for flexible electronics: a practical investigation on the electrical, film flexibility, optical, temperature, and solvent resistance properties. *J. Polym. Sci. Part B Polym. Phys.* **49**, 638–648 (2011).
8. Yin, Z. P. et al. Inkjet printing for flexible electronics: materials, processes and equipments. *Chin. Sci. Bull.* **55**, 3383–3407 (2010).
9. Gao, W. et al. Flexible electronics toward wearable sensing. *Acc. Chem. Res.* **52**, 523–533 (2019).
10. Kuzubasoglu, B. A. & Bahadir, S. K. Flexible temperature sensors: a review. *Sens. Actuators A Phys.* **315**, 112282 (2020).
11. Liu, Y. et al. Epidermal electronics for respiration monitoring via thermo-sensitive measuring. *Mater. Today Phys.* **13**, 100199 (2020).
12. Li, Q. et al. Review of flexible temperature sensing networks for wearable physiological monitoring. *Adv. Healthc. Mater.* **6**, 1601371 (2017).
13. Rufo, J. et al. A sound approach to advancing healthcare systems: the future of biomedical acoustics. *Nat. Commun.* **13**, 3459 (2022).
14. Gu, Y. et al. Acoustofluidic centrifuge for nanoparticle enrichment and separation. *Sci. Adv.* **7**, eabc0467 (2021).
15. Wu, M. et al. Sound innovations for biofabrication and tissue engineering. *Microsyst. Nanoeng.* **10**, 170 (2024).
16. Liu, Z. et al. A thin-film temperature sensor based on a flexible electrode and substrate. *Microsyst. Nanoeng.* **7**, 42 (2021).
17. He, Y. et al. Creep-free polyelectrolyte elastomer for drift-free iontronic sensing. *Nat. Mater* **23**, 1107–1114 (2024).
18. Su, Q. et al. A stretchable and strain-unperturbed pressure sensor for motion interference–free tactile monitoring on skins. *Sci. Adv.* **7**, eabi4563 (2021).

19. Liu, Z. et al. Influences of annealing temperature on the thermoelectric properties of thin film thermocouples based on a flexible substrate by RF magnetron sputtering. *Meas. Sci. Technol.* **31**, 095101 (2020).
20. Liu, Z. et al. A temperature sensor based on flexible substrate with ultra-high sensitivity for low temperature measurement. *Sens. Actuators A Phys.* **315**, 112341 (2020).
21. Lee, H. R., Kim, C. C. & Sun, J. Y. Stretchable ionics–a promising candidate for upcoming wearable devices. *Adv. Mater.* **30**, 1704403 (2018).
22. Zhang, Z. et al. Flexible thin film thermocouples: from structure, material, fabrication to application. *Iscience* **26**, 107303 (2023).
23. Rahman, M. T. et al. High performance flexible temperature sensors via nanoparticle printing. *ACS Appl. Nano Mater.* **2**, 3280–3291 (2019).
24. Han, D. et al. To save half contact pads in 2D mapping of local temperatures with a thermocouple array. *RSC Adv.* **7**, 9100–9105 (2017).
25. Zhao, X. et al. Preparation and thermoelectric characteristics of ITO/Pt thin film thermocouples on Ni-based superalloy substrate. *Vacuum* **140**, 116–120 (2017).
26. Liu, Z. et al. Flexible temperature sensor with high sensitivity ranging from liquid nitrogen temperature to 1200 °C. *Int. J. Extrem. Manuf.* **5**, 015601 (2023).
27. Liu, D. et al. Enhanced $La_{0.8}Sr_{0.2}CrO_3$/Pt thin film thermocouple with Al_2O_3 coating layer for high temperature sensing. *Ceram. Int.* **44**, S233–S237 (2018).
28. Okpalugo, T. I. T. et al. High resolution XPS characterization of chemical functionalised MWCNTs and SWCNTs. *Carbon* **43**, 153–161 (2005).
29. Arunkumar, T. et al. Synthesis and characterisation of multi-walled carbon nanotubes (MWCNTs). *Int. J. Ambient Energy* **41**, 452–456 (2020).
30. Kumar, A. et al. Thermo-mechanical and anti-corrosive properties of MWCNT/epoxy nanocomposite fabricated by innovative dispersion technique. *Compos. Part B Eng.* **113**, 291–299 (2017).
31. Fan, J. A. et al. Fractal design concepts for stretchable electronics. *Nat. Commun.* **5**, 3266 (2014).
32. Liu, Z. et al. High-performance temperature sensor by employing screen printing technology. *Micromachines* **12**, 924 (2021).
33. Jia, N. et al. Thermoelectric materials and transport physics. *Mater. Today Phys.* **21**, 100519 (2021).
34. Zhao, L., Wang, S. & Xiao, Y. Carrier mobility optimization in thermoelectric materials. *Acta Met. Sin.* **57**, 1171–1183 (2021).
35. Qin, Y., Xiao, Y. & Zhao, L. D. Carrier mobility does matter for enhancing thermoelectric performance. *APL Mater.* **8**, 010901 (2020).
36. Amaral, A. et al. ITO properties on anisotropic flexible transparent cellulosic substrates under different stress conditions. *Mater. Sci. Eng. B* **118**, 183–186 (2005).
37. Lan, Y. F. et al. Durability under mechanical bending of the indium tin oxide films deposited on polymer substrate by thermionically enhanced sputtering. *Org. Electron.* **11**, 670–676 (2010).
38. Grego, S. et al. Development and evaluation of bend-testing techniques for flexible-display applications. *J. Soc. Inf. Disp.* **13**, 575–581 (2005).
39. Hua, Q. et al. Skin-inspired highly stretchable and conformable matrix networks for multifunctional sensing. *Nat. Commun.* **9**, 244 (2018).
40. Wang, J. A. J. et al. A new approach for evaluating thin film interface fracture toughness. *Mater. Sci. Eng. A* **426**, 332–345 (2006).
41. Browning, G., Carlsson, L. A. & Ratcliffe, J. G. Modification of the edge crack torsion specimen for mode III delamination testing. Part II–experimental study. *J. Compos. Mater.* **45**, 2633–2640 (2011).
42. Oliveira, A. V. S., Avrit, A. & Gradeck, M. Thermocouple response time estimation and temperature signal correction for an accurate heat flux calculation in inverse heat conduction problems. *Int. J. Heat. Mass Transf.* **185**, 122398 (2022).
43. Tian, B. et al. A High-precision three-dimensional probe array temperature sensor. *Chemosensors* **10**, 309 (2022).
44. Luo, Y. et al. Technology roadmap for flexible sensors *ACS Nano* **17**, 5211–5295 (2023).
45. Cao, R. et al. Screen-printed washable electronic textiles as self-powered touch/gesture tribo-sensors for intelligent human–machine interaction. *ACS Nano* **12**, 5190–5196 (2018).
46. Shi, Q. et al. Deep learning enabled smart mats as a scalable floor monitoring system. *Nat. Commun.* **11**, 4609 (2020).
47. Popov, T. A., Kralimarkova, T. Z. & Dimitrov, V. D. Measurement of exhaled breath temperature in science and clinical practice. *Breathe* **8**, 186–192 (2012).
48. Folke, M. et al. Critical review of non-invasive respiratory monitoring in medical care. *Med. Biol. Eng. Comput.* **41**, 377–383 (2003).